Nano Research
2024, 17(4): 3087–3095

ISSN 1998-0124 CN 11-5974/O4
https://doi.org/10.1007/s12274-023-6175-z

Research Article

Polymer: Non-fullerene acceptor heterojunction-based phototransistor for short-wave infrared photodetection

Jing Li[1], Weigang Zhu[1] (✉), Yang Han[2], Yanhou Geng[2], and Wenping Hu[1] (✉)

[1] *Key Laboratory of Organic Integrated Circuits of Ministry of Education & Key Laboratory of Molecular Optoelectronic Sciences, School of Science & Collaborative Innovation Center of Chemical Science and Engineering (Tianjin), Tianjin University, Tianjin 300072, China*
[2] *Key Laboratory of Organic Integrated Circuits of Ministry of Education & Key Laboratory of Molecular Optoelectronic Sciences, School of Materials Science and Engineering, Tianjin University, Tianjin 300072, China*

Received: 17 August 2023 / **Revised:** 7 September 2023 / **Accepted:** 7 September 2023

ABSTRACT

It remains full of challenge for extending short-wave infrared (SWIR) spectral response and weak-light detection in the context of broad spectral responses for phototransistor. In this work, a novel poly(2,5-bis(4-hexyldodecyl)-2,5-dihydro-3,6-di-2-thienyl-pyrrolo[3,4-c]pyrrole-1,4-dione-alt-thiophene) (PDPPT3-HDO):COTIC-4F organic bulk-heterojunction is prepared as active layer for bulk heterojunction phototransistors. PDPPT3-HDO serves as a hole transport material, while COTIC-4F enhances the absorption of SWIR light to 1020 nm. As a result, smooth and connected PDPPT3-HDO film is fabricated by blade coating method and exhibits high hole mobility up to 2.34 $cm^2 \cdot V^{-1} \cdot s^{-1}$ with a current on/off ratio of 4.72×10^5 in organic thin film transistors. PDPPT3-HDO:COTIC-4F heterojunction phototransistors exhibit high responsivity of 2680 $A \cdot W^{-1}$ to 900 nm and 815 $A \cdot W^{-1}$ to 1020 nm, with fast response time (rise time ~ 20 ms and fall time ~ 100 ms). The photosensitivity of the heterojunction phototransistor improves as the mass ratio of non-fullerene acceptors increases, resulting in an approximately two orders of magnitude enhancement compared to the bare polymer phototransistor. Importantly, the phototransistor exhibits decent responsivity even under ultra-weak light power of 43 $\mu W \cdot cm^{-2}$ to 1020 nm. This work represents a highly effective and general strategy for fabricating efficient and sensitive SWIR light photodetectors.

KEYWORDS

photodetection, phototransistor, organic semiconductor, heterojunction, non-fullerene acceptor

Introduction

For a variety of industrial and scientific applications such as security systems, image sensing, communications, remote control, and chemical/biological sensing, near infrared (NIR) and short-wave infrared (SWIR) detection is required [1–4]. The typical detectors based on Si-, GaN-, and InGaAs have the advantages of high sensitivity, high quantum efficiency and high speed [5–7]. However, to achieve high detectivity for most inorganic-based infrared detectors, extra cooling equipment is required to reduce dark current, which fundamentally limits their wide application scenarios. Besides, inorganic materials are inherently rigid, which is unsuitable for flexible and wearable electronics era [8, 9].

Considering the limitations mentioned above, novel materials are important factor driving innovation. Among the emerging materials for optoelectronic devices, organic semiconductors have gained significant attention [10–15]. In comparison to their inorganic counterparts, organic-based NIR and SWIR photodetectors exhibit marked advantages of cooling-free system. They also exhibit inherent flexible properties, light weight, low price and low-temperature processability. Furthermore, the absorption window of organic materials can be fine-tuned by tailoring the chemical structure. Thus, they have great potential for application in wearable electronics and real-time human health monitoring [16, 17]. In the past few decades, more and more novel polymers with high mobility and small molecules with narrow optical bandgaps materials have been exploited for the use as active layer. Polymer, poly(2,5-bis(4-hexyldodecyl)-2,5-dihydro-3,6-di-2-thienyl-pyrrolo[3,4-c]pyrrole-1,4-dione-alt-thiophene) (PDPPT3-HDO), with high hole mobility 9.24 $cm^2 \cdot V^{-1} \cdot s^{-1}$ has been reported [18]. Non-fullerene acceptors (NFAs) with narrow bandgaps, tunable energy levels and crystallinity exhibit great performance in organic photodetectors and organic photovoltaics (OPVs) [19–21]. COTIC-4F, a typical NFA with narrow bandgap as low as 1.10 eV, has been reported to exhibit power conversion efficiencies of up to 9.0% when blending with PTB7-Th in OPV [22]. In general, exciton dissociation in organic semiconductors is difficult due to their small dielectric constant and high exciton binding energy [23]. However, in bulk heterojunction, the interface between donor and acceptor promotes efficient exciton dissociation and transfer of photogenerated carriers. This strategy has been pursed to achieve highperformance photodetectors [24, 25]. Consequently, heterostructure phototransistors (OPTs) have been employed for photodetection [26]. Literature has reported the integration of organic ternary bulk heterojunction as photosensitive layer, with responsivity of 6.1×10^6 $A \cdot W^{-1}$ for 850 nm [27]. In_2O_3/PTPBT-ET hybrid phototransistors show high responsivity of 200 $A \cdot W^{-1}$, and specific detectivity of 1.2×10^{13} Jones of 810 nm NIR light [28]. OPTs possess several advantages

Address correspondence to Weigang Zhu, w_zhu10@tju.edu.cn; Wenping Hu, huwp@tju.edu.cn

over photodiode, including extremely low noise current, exceptionally high responsivity and photoconductive gain. High mobility materials such as graphene and In_2O_3 are used as electron transport channel. Generally, the performance of organic phototransistor is restricted by absorption window of active layer and mobility for carrier transport.

Herein, we demonstrate a high-performance short-wave infrared phototransistor, employing bulk heterojunction, combining high mobility p-type polymer and a wide optical absorption spectra non-fullerene acceptor, as photosensitive layer. As a result, our PDPPT3-HDO:COTIC-4F heterojunction phototransistors exhibit high responsivity of 2680 $A \cdot W^{-1}$ to 900 nm and 815 $A \cdot W^{-1}$ to 1020 nm, with fast response time (rise time ~ 20 ms and fall time ~ 100 ms). Furthermore, we find that the photoresponse improves as the concentration of non-fullerene acceptors increases. Importantly, the phototransistors exhibit decent photoresponse even under ultra-weak light intensity of 43 $\mu W \cdot cm^{-2}$. Overall, the performance of the organic phototransistors is superior to the most reported organic infrared phototransistors. This strategy provides an effective method for the fabrication of low-cost and high-performance infrared optoelectronic devices.

2 Results and discussion

2.1 Optical absorption and energetics

As shown in Fig. 1(a), PDPPT3-HDO and COTIC-4F are blended in 1,2-dichlorobenzene (o-DCB) solution. The molecular structures of PDPPT3-HDO and COTIC-4F are displayed in Fig. 1(b). Long alkyl group between branching point and backbone in PDPPT3-HDO molecule can reduce steric hindrance and facilitate close cofacial π–π stacking. COTIC-4F is a narrow bandgap NFA molecule with an electron-rich internal core and acceptor units as termini. As shown in Fig. 1(c), PDPPT3-HDO is a typical narrow optical bandgap polymer with strong absorption from 400 to 984 nm, absorption of COTIC-4F film is from 400 to 1250 nm. COTIC-4F in the PDPPT3-HDO:COTIC-4F helps to broaden the optical absorption spectra. The optical bandgaps (E_g) of PDPPT3-HDO and COTIC-4F are estimated to be 1.29 and 0.99 eV from the adsorption onset, respectively. Therefore, PDPPT3-HDO film can absorb most visible and NIR photons (400–984 nm), while organic bulk heterojunction (BHJ) film can efficiently utilize NIR and SWIR light (400–1250 nm). The heterojunction film significantly extends SWIR spectral response compared with PDPPT3-HDO film.

The energy levels of PDPPT3-HDO and COTIC-4F are analyzed using ultraviolet photoelectron spectroscopy (UPS). The highest occupied molecular orbital (HOMO) levels are obtained by the valence band edges and the secondary electron cutoff (Figs. 1(d) and 1(e), and Fig. S1 in the Electronic Supplementary Material (ESM)). The HOMO levels of the PDPPT3-HDO and COTIC-4F are −4.76 and −5.14 eV (Table 1), respectively, and the lowest unoccupied molecular orbital (LUMO) levels are determined by combining the optical bandgap values obtained from the ultraviolet–visible (UV–vis) absorption spectra (Fig. 1(c)) with the HOMO levels. The LUMO levels of PDPPT3-HDO and COTIC-4F are −3.98 and −4.15 eV (Table 1), respectively. Figure S2 in the ESM shows the cyclic voltammograms (CV) of PDPPT3-HDO, COTIC-4F and the ferrocene standard redox couple. According to the onset potentials of oxidation, the HOMO energy levels of PDPPT3-HDO and COTIC-4F are estimated to be −5.27 and −5.21 eV, respectively. We have identified a type II band alignment between PDPPT3-HDO and COTIC-4F. The energy alignment in a type-II heterojunction forms a staggered gap. The highest occupied molecular orbital and lowest unoccupied molecular orbital of PDPPT3-HDO are higher than the corresponding energy levels of COTIC-4F in heterojunction. This type of band alignment could substantially reduce the electron concentration within the heterojunction, leading to a reduction in charge recombination at the interface of donor and acceptor. Moreover, the type of heterojunction promotes the extraction of hole into the PDPPT3-HDO layer due to the band bending [29, 30]. Due to the low LUMO energy levels of COTIC-4F, it is expected that NFAs will efficiently generate charge in blended film. Their energy offset is enough to separate the electron–hole pairs (Fig. 1(f))

2.2 Film processing, optimization, and morphology

In order to understand the influence of the different acceptor concentrations on the thin film morphology, solutions of various ratio PDPPT3-HDO:COTIC-4F blends dissolved in o-DCB are blade-coated on Si/SiO_2 substrates at various temperatures. Characterization of PDPPT3-HDO:COTIC-4F blended films shows that all films with different ratios display favorable phase separation of PDPPT3-HDO and COTIC-4F. Well phase separation facilitates to balanced transport of carriers in interconnected network, shortened distance of exciton diffusion and enhanced excitons dissociation [31]. The thicknesses of blade coated PDPPT3-HDO:COTIC-4F films ranged from ~ 40 to 70 nm, as shown in the height profiles from atomic force microscopy (AFM) images (Fig. 2(a) and Fig. S3 in the ESM). The surface smoothness of the PDPPT3-HDO:COTIC-4F films is relatively smooth, with low surface roughness root mean square (RMS) values raging from ~ 9.2 to 28.7 nm. The smooth surface morphology is beneficial to suppress surface scattering, increase light absorption and reduce the generation of trap states [32].

In view of the distribution of the two components in the blended films, a surface-sensitive technique, X-ray photoelectron spectroscopy (XPS) is used to provide a more comprehensive chemical picture. As shown in Fig. 2(b), the peaks at 284.8 and 286.43 eV obtained by peak fitting suggest the C–C and C=N bonding formation of sp^2-C atoms and sp^3-C atoms with nitrogen atoms, respectively [33–36]. Compared with the pristine PDPPT3-HDO, there is considerable COTIC-4F in W-1.5, W-3 as evidenced by the appearance of the new C 1s binding peaks at approximately 285.51 and 285.78 eV. The C–N peak positions of W-1.5 and W-3 shift to higher binding energy compared with the corresponding peak of PDPPT3-HDO. According to C1s XPS spectra, the peak area ratio of compositions of C=N to C–N and C=C keeps increasing (from 7.0% to 10.6%) with an increasing amount of COTIC-4F in W-1.5 and W-3. XPS survey confirms the present of the C, S and N elements in PDPPT3-HDO and COTIC-4F (Fig. S4 in the ESM).

Next, we compared the UV–vis absorption changes of bare PDPPT3-HDO film and hybrid films with the addition of various concentration of COTIC-4F, as shown in Fig. 2(c). The results reveal that an increase in the mass ratio of COTIC-4F correlates with a rise in absorption in the short-wave infrared region. It is highly expected to achieve a high photocurrent output under SWIR light. In addition, grazing-incidence X-ray diffraction (GIXRD) of the films show that the PDPPT3-HDO films exhibit higher crystallinity compared to the blended PDPPT3-HDO:COTIC-4F films (Fig. 2(d)). Interestingly, we observe distinct differences in the peak intensity of the X-ray diffraction patterns, which is indicative of the spatial number density of the crystallites. Specifically, the blend films show lower peak intensity suggesting the entropy-driven disorder caused by the addition of COTIC-4F [37, 38].

Materials with high mobility allow photogeneration carriers to recirculate in channel before recombination with electrons

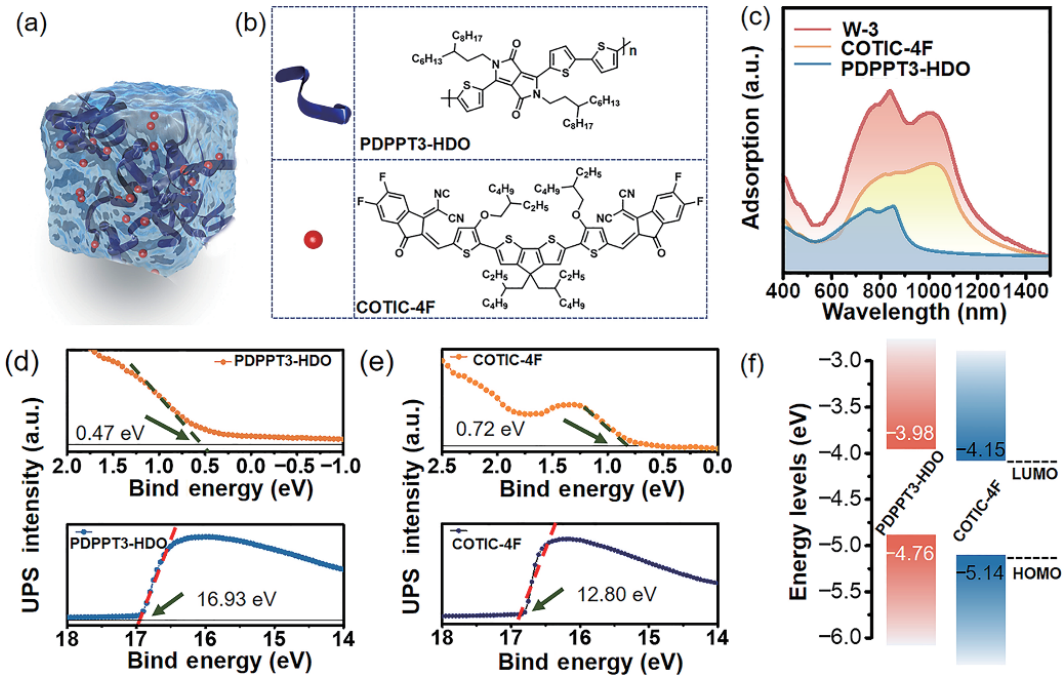

Figure 1 (a) The mimetic diagram of PDPPT3-HDO and COTIC-4F in o-DCB solution. (b) Molecular structures of PDPPT3-HDO and COTIC-4F. (c) UV–vis absorption spectra of PDPPT3-HDO film, COTIC-4F film, and PDPPT3-HDO/COTIC-4F blended film (W-3). UPS spectra of the valence band region and the secondary electron cutoff region of (d) PDPPT3-HDO and (e) COTIC-4F. (f) Band alignment of PDPPT3-HDO and COTIC-4F heterojunction, which is type-II heterojunction and beneficial to exciton dissociation and transportation

Table 1 Electronic properties of PDPPT3-HDO and COTIC-4F

Sample (eV)	Cutoff tail	Fermi tail	HOMO	HOMO(CV)	LUMO	E_g
PDPPT3-HDO	16.93	0.47	−4.76	−5.27	−3.98	1.29
COTIC-4F	16.80	0.72	−5.14	−5.10	−4.15	0.99

trapped in COTIC-4F. Consequently, promoting mobility of PDPPT3-HDO is facilitated to enhance the photosensitivity. Figure S5 in the ESM shows a schematic diagram of PDPPT3-HDO film fabrication with blade coating method. During solution shearing, OSC solution is across a heated substrate and solution shearing conditions change the molecular packing of polymer [39]. The polarized optical microscopy (POM) images at polarized angle of 45° of PDPPT3-HDO films prepared at substrate temperature of 60 °C, show constant brightness; however, the brightness of PDPPT3-HDO films prepared at substrate temperature of 80–120 °C is extinguished (Fig. S6 in the ESM). This result demonstrates that high substrate temperature facilitates

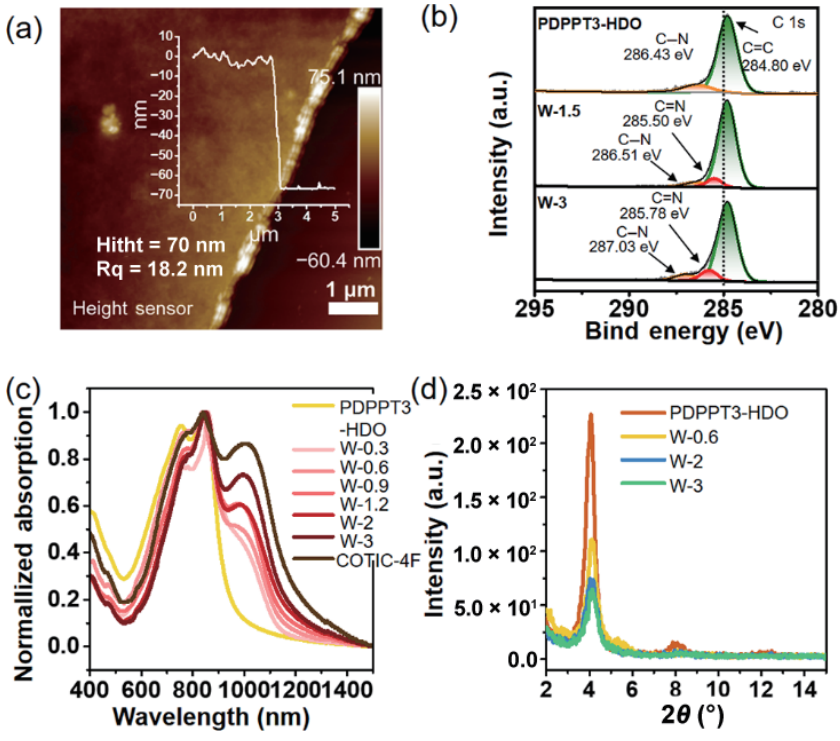

Figure 2 Film morphology and phase separation. (a) Typical tapping-mode AFM height image of PDPPT3-HDO:COTIC-4F thin blade-coating films at substrate temperatures of 120 °C. (b) C 1s high-resolution XPS spectra of PDPPT3-HDO and W-1.5, W-3 blended films. (c) UV–vis absorption spectra of various blended films. (d) GIXRD spectra of PDPPT3-HDO, W-0.6, W-2 and W-3 films.

the formation of highly aligned and highly ordered polymer films. AFM is used to characterize the surface morphology of the thin films. Figure S7 in the ESM depicts the AFM topographical images of films casted with solution concentration of 2, 4 and 6 mg·mL^{-1}, respectively. The thin films casted by solution of 2 and 4 mg·mL^{-1} do not form well-connected films (Figs. S7(a)–S7(d) in the ESM). The poor connection between domains potentially results in low charge carrier mobility. Conversely, films casted with solution concentration of 6 mg·mL^{-1} formed smooth and connected films (Fig. S7(e) in the ESM). GIXRD was performed on the polymer thin films for more insight into the structure. PDPPT3-HDO exhibits small full width at half maximum (FWHM) of 0.057, indicating a high level of molecular ordering (Fig. S8 in the ESM) [40, 41]. Ordered molecular arrangement facilitates electronic overlap between molecules, which can increase the carrier mobility. Thus, PDPPT3-HDO film is highly anticipated to achieve a high mobility.

2.3 Field-effect transistor (FET) and phototransistor measurements

The electronic properties of PDPPT3-HDO thin-film as a solution-processed semiconductor layer are evaluated using a bottom-gate, top-contact FET configuration which is schematically illustrated in Fig. 3(a). The active layer of PDPPT3-HDO is blade-coated on octadecyltrchlorosilane (OTS) modified Si/SiO_2 substrates, with a concentration of 6 mg·mL^{-1} in o-DCB. More details are described in the Experimental section. Figures 3(b) and 3(c) show the typical transfer and output curves. The transfer characteristics show a typical p-type semiconductor behavior, threshold voltage as small as 4.2 V and the optimized mobility of 2.34 cm^2·V^{-1}·s^{-1} with a current on/off ratio of 4.72 × 10^5. The output behaviors exhibit good saturation and no observable contact resistance. Figure 3(d) illustrates the mobility distribution of PDPPT3-HDO film-based organic field-effect transistors (OFETs). Substrate temperatures, solution concentration and blade speed influence the electronic properties of polymer as well. Mobility of PDPPT3-HDO exhibits a significant enhancement at elevated with substrate temperature. As shown in Fig. S9 in the ESM, the highest mobilities are achieved at substrate temperatures of 80 °C (1.15 cm^2·V^{-1}·s^{-1}), 100 °C (1.05 cm^2·V^{-1}·s^{-1}), and 120 °C (2.14 cm^2·V^{-1}·s^{-1}), respectively. If substrate temperature is further increased, the PDPPT3-HDO films exhibit poor connection domain, hindering the hole transport in films.

In order to investigate the photoresponses of bare PDPPT3-HDO film based devices to NIR light, light illumination with wavelength of 900 and 1020 nm at various power density is applied on devices, and the transfer curves are shown in Fig. 4(a) and Fig. S10 in the ESM, respectively. Light source (λ = 900 and 1020 nm) is carried with Zolix MLED4-3. Power intensity was calibrated *in situ* with a PM100 digital power meter. As shown in Fig. 4(a), PDPPT3-HDO phototransistor exhibits off-current increase under light illumination of 900 nm. Meanwhile, Fig. 4(d) displays the dependence of responsivity (R) and specific photodetectivity (D^*) values on gate voltage. As the light power changing, the max values of R and D^* are achieved to ~ 61 A·W^{-1} and 2.7 × 10^7 Jones. In regards to photoresponse to 1020 nm, the PDPPT3-HDO phototransistor exhibits no significant change in transfer characteristics under light illumination of 1020 nm, which is due to the large bandgap of PDPPT3-HDO (1.29 eV) (Fig. S10 in the ESM).

As for the electronic properties of PDPPT3-HDO:COTIC-4F heterojunction transistor, the field-effect mobility extracted at gate voltage (V_G) of −40 V in saturated region shows that the heterojunction phototransistor has a significantly reduced mobility of ~ 0.1 cm^2·V^{-1}·s^{-1} as compared to the PDPPT3-HDO transistor (2.34 cm^2·V^{-1}·s^{-1}). It can be attributed to that the incorporation of COTIC-4F forms the scattering centers of hole and hinders holes transport in the channel. The dark off-current increases with the enhanced COTIC-4F concentration.

2.4 SWIR photodetection

The PDPPT3-HDO:COTIC-4F phototransistor shows significant negative V_{TH} shifts together with off-current increase under light illumination of 900 and 1020 nm, indicating the strong SWIR and

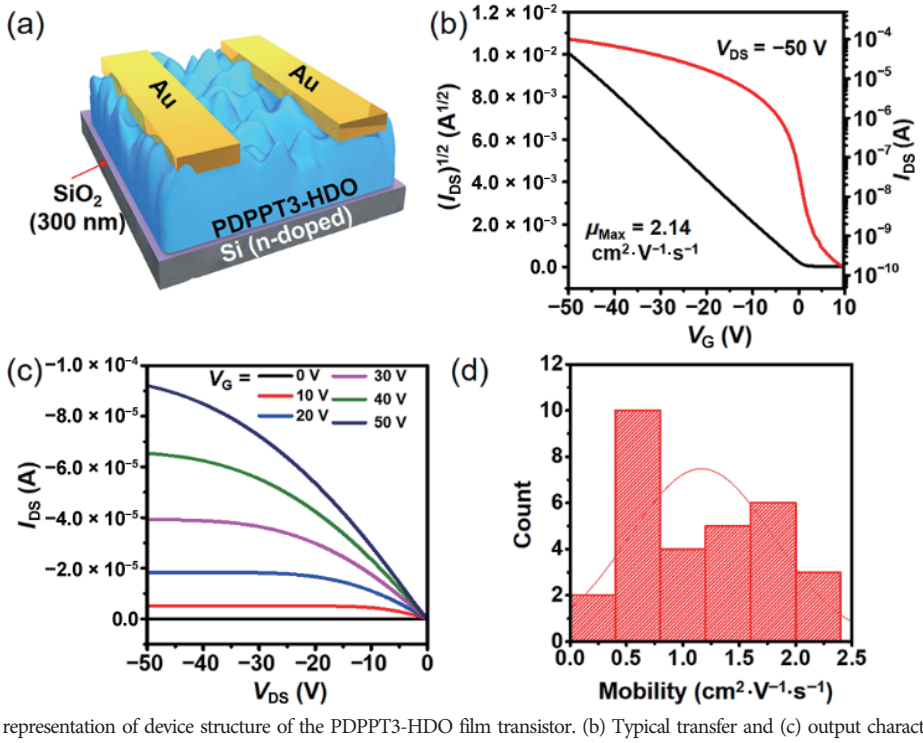

Figure 3 (a) Schematic representation of device structure of the PDPPT3-HDO film transistor. (b) Typical transfer and (c) output characteristics of OFET devices based on PDPPT3-HDO blade-coating film from o-DCB solution in parallel direction. The substrate temperature is set to 120 °C, with a blade speed of 0.67 mm·s^{-1}, an angle of 25° between the scraper and substrate. (d) The mobility distribution of PDPPT3-HDO film OFETs.

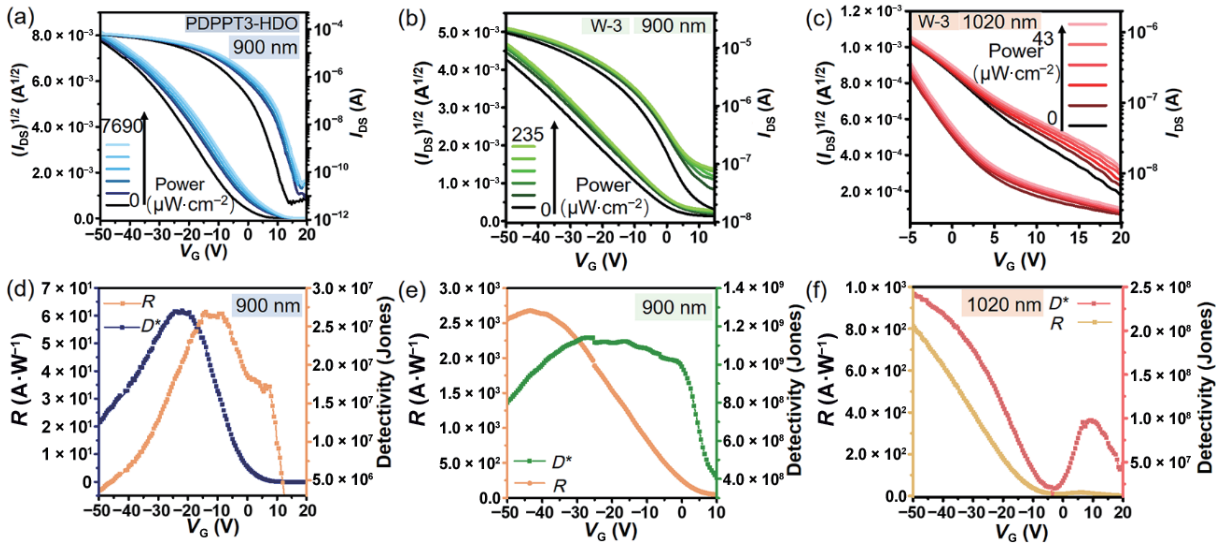

Figure 4 Phototransistor in dark and under illumination: (a) PDPPT3-HDO film phototransistor in dark and under 900 nm, (b) W-3 phototransistor in dark and under 900 nm and (c) W-3 phototransistor in dark and under 1020 nm. Dependence of *P* and *R* on the gate voltage with (d) PDPPT3-HDO film phototransistor under 7690 μW·cm^{-2} illumination of 900 nm (source-drain voltage V_{DS} = −50 V), (e) W-3 phototransistor under 235 μW·cm^{-2} illumination of 900 nm (V_{DS} = −50 V) and (f) W-3 phototransistor under 43 μW·cm^{-2} illumination of 1020 nm (V_{DS} = −50 V).

NIR photoresponse. To evaluate the performance of heterojunction phototransistors, we examined the photoresponse at various power density ranging from 0 to 235 μW·cm^{-2} of 900 nm and ranging from 0 to 43 μW·cm^{-2} of 1020 nm. Figures 4(b) and 4(c) display the typical transfer characteristics of a phototransistor based on the W-3 blend film, which exhibits a typical p-type behavior. Here, V_G is swept from 20 to −50 V while keeping V_D fixed at −50 V. Upon light absorption, electron–hole pairs are generated in the PDPPT3-HDO:COTIC-4F blended film. Holes transfers to polymer with high mobility, contributing to the photocurrent. Simultaneously, the electrons are trapped by NFAs, which effectively delays the recombination of photogenerated charge carriers. The short transit time for carriers, along with long recombination time of photogeneration carriers, is benefit to gain large photogain [42, 43]. It is obvious that source-drain current (I_{DS}) shows a noticeable increase with light illumination power increase with both 900 and 1020 nm wavelengths, indicating that the photoactive layer efficiently generates free-charge carriers. Furthermore, the threshold voltage (V_{TH}) exhibits a positive shift, which is attributed to the photogating effect induced by the trapping of photoelectrons in COTIC-4F.

The photodetection characteristics of the PDPPT3-HDO:COTIC-4F heterojunction phototransistor are systematically evaluated. Phototransistors are named as W-0.3, W-0.6, W-0.9, W-1.2, W-2, and W-3, which are prepared with PDPPT3-HDO:COTIC-4F blend films with weight ratio of 1:0.3, 1:0.6, 1:0.9, 1:1.2, 1:2 and 1:3, respectively. In order to investigate the influence of mass ratio of COTIC-4F on photoresponse of phototransistor, we further increased the concentration of COTIC-4F in blended film. As the illustration of Figs. S11 and S12 in the ESM, with the mass ratio $m_{(PDPPT3-HDO)}$:$m_{(COTIC-4F)}$ increasing from 1:0.6 to 1:3, dark current (I_{dark}) increases. Specifically, W-0.6 presents the lowest I_{dark} of 1.12 × 10^{-9} A, while I_{dark} increases to 1.6 × 10^{-8} A in W-3. The dark current in organic bulk heterojunction photodetectors is mainly influenced by charge injection barrier and spatial distribution of donors and acceptors. Here, we used unmodified electrodes without an electron blocking layer, which makes charge injection from electrodes to COTIC-4F phase relatively easy [44, 45]. The absence of an electron-blocking layer allows electron injection, which contributing to a high dark current. High concentration COTIC-4F based phototransistors exhibit high V_{TH} and high dark current, which could be attributed to the facilitated injection of electrons into active layer by COTIC-4F. Additionally, the phase separation of donors and acceptors may insufficient, it can lead to inefficient charge transport and increased carrier recombination, resulting in a high dark current [46]. The photosensitivity (I_{photo}/I_{dark}, *P*) of the phototransistor is studied as a function of V_G for varying light power. Generally, I_{photo}/I_{dark} in the off-state is higher than that in the on-state. Because the charge carriers in the phototransistors are mainly modulated by the incident light at the turn-off gate voltage, where the maximum I_{photo}/I_{dark} is observed. The maximum I_{photo}/I_{dark} obtained fromW-3 is 4.16 with incident light power of 235 μW·cm^{-2} of 900 nm (Table 2, and Fig. S12 and Table S1 in the ESM).

R of other phototransistors is similar, while *R* of the phototransistors are obviously different related with concentration of COTIC-4 (Fig. S12 in the ESM). *R* indicates the electrical signal that a device reaches under a certain illumination power. Besides, the increase in *R* with V_G can be attributed to the influence of the vertical electric field on enhancing the efficiency of exciton dissociation [47]. Therefore, photosensitivity can be effectively adjusted by both the incident light power and gate voltage. The calculated responsivity shows an increasing trend with increasing of COTIC-4F. The highest *R* for W-0.6, W-2 and W-3 are about 754, 932 and 2680 A·W^{-1}, respectively. According to the report, *R* is also influenced by *W*/*L* value, with a high *W*/*L* value resulting in a high R. In this study, we maintain the *W*/*L* value at 8, which is lower compared to Ref. [48]. The present of COTIC-4F trapped electrons and induced band bending at the interface, which enhances hole injection from the external circuit [49]. Therefore, the increased *R* value of the phototransistors in this work is attributed to the increase in the number of photogenerated carriers. The peak of *D** for W-0.6, W-2 and W-3 under irradiation is above 10^8 Jones. Substrate temperature also influences the phototransistor performance. We find that compared with active layer of W-3 prepared at 80 and 100 °C, active layer prepared at 120 °C exhibits the best photosensitivity performance. As shown in Fig. S11 in the ESM, the specific photodetectivities of W-3 with active layer prepared at 80, 100 and 120 °C are 892, 1511 and 2680 Jones, respectively. Photoresponse of W-0.6 and W-2 phototransistor with active layer prepared at different substrate temperatures is listed in Table S1 in the ESM.

Table 2 The maximum value of mobility, sensitivity, responsibility and detectivity of 900 nm obtained from PDPPT3-HDO, W-0.6, W-2, and W-3 phototransistor prepared with substrate temperature of 120 °C

Samples	Mobility ($cm^2 \cdot V^{-1} \cdot s^{-1}$)	P	R ($A \cdot W^{-1}$)	D^* (Jones)
PDPPT3-HDO	2.34	556	61.78	2.68×10^7
W-0.6	0.34	1.61	754.1	2.33×10^8
W-2	0.17	6.89	932.0	3.58×10^8
W-3	0.24	4.16	2680	1.14×10^9

Higher temperature of substrate enables polymer chains to adjust their conformation during film formation, leading to enhanced polymer crystallinity and forming domain of small size, which facilitates exciton dissociation [50]. The mobilities of blended film prepared at different temperature are similar.

2.5 Weak SWIR light detection

Detection of weak light is critical to many applications. Heterojunction phototransistors with the low mobility and high dark off-current achieve well photoresponse to weak light detection. As shown in Figs. 4(c) and 4(f), and Fig. S13 in the ESM, the R of the phototransistor based on W-0.3, W-0.6, W-0.9, W-1.2, W-2 and W-3 is 107, 499, 374, 15, 209 and 815 $A \cdot W^{-1}$, respectively, with incident light power of 43 $\mu W \cdot cm^{-2}$ at 1020 nm. Blended films with large ratio of NFAs forms well phase separation, offering extensive donor–acceptor interfaces to decrease hole–electron recombination and enhance effective hole–electron pair dissociation [51]. As a result, W-3 phototransistor has a maximum responsivity of 815 $A \cdot W^{-1}$ and D^* of 2.45×10^8 Jones, which exhibits outstanding photodetection characteristics under weak light illumination of 43 $\mu W \cdot cm^{-2}$. D^* is influenced by R and I_{dark}, and R is influenced by $I_{light} - I_{dark}$, where I_{light} is the current under illumination. I_{dark} changes slightly when the gate voltage is less than −35 V, the tendency of D^* increase can be attributed to I_{light} which is not saturated under the weak power (0.43 $\mu W \cdot cm^{-2}$) at 1020 nm. The trend of D^* decreasing and then increasing is mainly influenced by the term $(I_{light} - I_{dark})(I_{dark})^{-1/2}$, which is strongly influenced by the change of I_{dark} ($20 V \geq V_G \geq -4$ V). I_{dark} gains a lowest value when phototransistor is at the off state, resulting in the highest value of D^* at $20 V \geq V_G \geq -4$ V.

Figure S14 in the ESM shows the relationship between the V_{TH} and the incident light power with incident wavelength of 1020 nm for heterojunction phototransistors based on blended films. As the incident light power increases, the V_{TH} shifts towards positive voltage. The relatively slight small shift is due to the small increase of the incident light power. The V_{TH} shift in p-type phototransistors, is attributed to the higher carrier density under incident light, and further enhanced by electrons trapping in acceptor.

In order to investigate the optical on/off modulation of the phototransistors under the incident light, the channel current was mentioned. The drain current of W-0.3, W-0.6, W-0.9, W-1.2, W-2, and W-3 phototransistors at $V_G = V_{DS} = -10$ V exhibits a higher response to the incident light power of 43 $\mu W \cdot cm^{-2}$ than 28 $\mu W \cdot cm^{-2}$ (Fig. S15 in the ESM). Besides, persistent photoconductivity is observed in heterojunction phototransistors. Drain current of phototransistor sustains for a while after illumination. Some novel applications are based on the persistent photoconductivity for memory and imaging [52, 53]. Persistent photoconductivity is caused by defects which trap the photo-generated carriers at the interface. Besides, the active functional groups (–OH, $–NH_2$, –COOH, etc.) in polymers can also trap the photogenerated carriers [54, 55]. Persistent photoconductivity is also observed in PDPPT3-HDO:COTIC-4F heterojunction phototransistor, which is caused by abundant grain boundaries and traps caused by introduction of NFAs. By comparing our results with the literatures, we have found that our PDPPT3-HDO:COTIC-4F heterojunction phototransistors exhibit higher responsivity and faster raise time (Table S3 in the ESM).

Figure S16 in the ESM presents the short-term photocurrent signals of W-0.3, W-0.6, W-0.9, W-1.2, W-2, and W-3 heterojunction phototransistors under the 1020 nm light. According to the I_{DS}–t curves, the rise and decay times for the W-0.3 phototransistor are determined to be 0.29 and 0.10 s, respectively. The rise time for the W-0.6, W-0.9, W-1.2, W-2, and W-3 heterojunction transistors ranges from 0.025 to 0.051 s, while the decay times range from 0.07 to 0.13 s. It is worth noting that the rise time of films blended with large ratio of NFAs is lower than W-0.3 by an order of magnitude. Response speeds of PDPPT3-HDO:COTIC-4F heterojunction phototransistor is relatively fast compared to Refs. [32, 56].

3 Conclusions

In conclusion, an effective method to obtain a wide spectrum response of the polymer:non-fullerene acceptors phototransistor is proposed by integration of high-mobility polymer PDPPT3-HDO and narrow band acceptor COTIC-4F as active layer for organic heterojunction phototransistor. Mobility of polymer PDPPT3-HDO reaches 2.34 $cm^2 \cdot V^{-1} \cdot s^{-1}$. The heterojunction films extend photoresponse of the phototransistor to 1020 nm. The influence of substrate temperature and mass ratio on the photoresponse are investigated. The maximum responsivity of PDPPT3-HDO:COTIC-4F heterojunction (W-3) phototransistor is obtained at substrate temperature of 120 °C is 2680 $A \cdot W^{-1}$ (900 nm) and 815 $A \cdot W^{-1}$ (1020 nm). With mass ratio increasing, responsivity and specific detectivity of infrared light are enhanced. Finally, the introduction of COTIC-4F exhibits outstanding photoresponse for the SWIR weak light detection (43 $\mu W \cdot cm^{-2}$) to 1020 nm, with responsivity of 815 $A \cdot W^{-1}$ and specific detectivity of 2.45×10^8 Jones. The present study is expected to make a significant contribution to the development of high-sensitivity heterojunction phototransistors for short-wave infrared photodetection.

4 Experiment

4.1 Materials

All reagents and chemicals were obtained from commercial sources and used without further purification. COTIC-4F was purchased from Nanjing Zhiyan Technology Co., Ltd. PDPPT3-HDO was synthesized by us. OTS (CAS:112-04-9(8113), 95%) was purchased from Macklin. o-DCB (99%) and octadecyltrichlorosilane (95%) were purchased from Beijing InnoChem Science & Technology Co., Ltd. Si/SiO_2 (300 nm) substrates were purchased from 46th Research Institute affiliated with China Electronics Technology Group Corporation. Gold (purity of 99.999%) was purchased from ZhongNuo Advanced Material (Beijing) Technology Co., Ltd.

4.2 Device fabrication

Before fabrication, the Si/SiO_2 substrates were precleaned by in an ultrasonic bath of water, acetone, isopropanol, acetone, and isopropanol (each sonicated for 10 min). Afterwards, the substrates were dried with N_2 flow. Following the cleaning step, the substrates were cleaned under O_2 plasma with power of 80 W for 10 min. This was followed by a modification process with monolayer OTS. The purpose of the OTS modification was to

minimize the presence of traps and water molecules on the surface of substrates [57–59]. The semiconductor layer was deposited by blade coating using an o-DCB solution at a concentration of 6.0 mg·mL^{-1} at a speed of 0.67 cm·s^{-1}. To fabricate bulk heterojunction films, PDPPT3-HDO:COTIC-4F blend solution with weight ratio of 1:0.3, 1:0.6, 1:0.9, 1:1.2, 1:2 and 1:3 at 6 mg·mL^{-1} in o-DCB was blade-coated on the substrate. Subsequently, the films were thermally annealed for 3 h at 90 °C in nitrogen atmosphere. Then, Au (30 nm) was vacuum-evaporated on the films as source and drain electrodes with an interdigitated electrode pattern. Phototransistors were named as W-0.3, W-0.6, W-0.9, W-1.2, W-2, and W-3, which were prepared with PDPPT3-HDO:COTIC-4F blend films with weight ratio of 1:0.3, 1:0.6, 1:0.9, 1:1.2, 1:2 and 1:3, respectively.

4.3 Characterization of materials and electric properties

Optical and cross-polarized light microscope images were acquired using a Nikon Eclipse Ci-POL polarizing optical microscope. X-ray diffraction (XRD) and grazing incidence X-ray diffraction measurements were performed in reflection mode at 45 kV and 200 mA with monochromatic Cu Kα radiation utilizing a Rigaku Smartlab diffractometer. AFM was performed in intelligent mode with a Bruker Dimension Icon microscope. The UV–vis spectra were measured by a SHZMADZU UV-3600 Plus spectrophotometer. XPS and UPS measurements were conducted on a Thermo Scientific Escalab 250Xi ultra photoelectron spectrometer. He I photo source ($h\nu$ = 21.22 eV) was used as measurement. The electrical characteristics were measured by a Keithley 4200-SCS semiconductor parameter analyzer connected at room temperature. CV measurements were performed on a CHI600A electrochemical workstation with a three-electrode cell in 0.1 mol·L^{-1} tetrabutylammonium hexafluorophosphate (n-Bu_4NPF_6) acetonitrile solution. Ferrocene/ferrocenium redox couple was used as an internal standard at a scan rate of 50 mV·s^{-1}. The Ag/Ag$^+$ electrode, a platinum wire and an indium tin oxide (ITO) was used as the reference electrode, counter electrode, and working electrode, respectively. FETs were measured in air and at room temperature using a Keithley 4200-SCS. A TTPX Cryogenic probe station was used. Here, the mobility (μ) of devices was calculated with the equation: $I_{DS} = (W/2L)C_i\mu(V_G - V_{TH})^2$, where L and W were the channel length and width respectively, C_i was the oxide capacitance of 10 nF·cm^{-2}, V_{DS} was the drain to source bias [60–62]. Light source (λ = 900 and 1020 nm) was carried with Zolix MLED4-3. Power intensity was calibrated *in situ* with a PM100 digital power meter.

4.4 Essential parameters for phototransistor

Essential parameters including responsivity (R), specific detectivity and photosensitivity were figure-of-merit of photodetector [32]. The responsivity indicates the electrical signal under a certain illumination power. According to the equation: $R = (I_{light} - I_{dark})/PA = I_{ph}/PA$, where I_{dark} and I_{light} were the device output current without and with illumination, respectively, A refered to the area of channel, P was the light intensity [32, 63]. Photocurrent I_{ph} was defined as device current under illumination with absolute value, which was calculated as $I_{ph} = |I_{light} - I_{dark}|$. Specific detectivity ($D^*$) is an essential parameter for weak light detection. When the only current noise origins from dark current, D^* can be expressed as $D^* = RA^{1/2}(2qI_{dark})^{-1/2}$, where q *was* the element charge [64, 65].

Acknowledgements

This work was financially supported by the Ministry of Science and Technology of China (Nos. 2017YFA0204503 and 2018YFA0703200), the National Natural Science Foundation of China (Nos. 52121002, 51733004, 51725304, 21875158, and U21A6002), Tianjin Natural Science Foundation (No. 20JCJQJC00300) and the Discretionary Fund of Tianjin University (No. 2104).

Electronic Supplementary Material: Supplementary material (UPS spectra and CVs of PDPPT3-HDO and COTIC-4F, AFM images of PDPPT3-HDO films and PDPPT3-HDO:COTIC-4F blended films, XPS spectra of PDPPT3-HDO films and blended films, polarized optical microscopy images of PDPPT3-HDO films, GIXD patterns of PDPPT3-HDO films and blended films, transfer curves of PDPPT3-HDO films at different substrate temperature, phototransistor based on PDPPT3-HDO films and blended films, photoresponse characteristics of PDPPT3-HDO:COTIC-4F heterojunction phototransistor, time-dependent photoresponse of heterojunction phototransistor) is available in the online version of this article at https://doi.org/10.1007/s12274-023-6175-z.

References

[1] Gong, X.; Tong, M. H.; Xia, Y. J.; Cai, W. Z.; Moon, J. S.; Cao, Y.; Yu, G.; Shieh, C. L.; Nilsson, B.; Heeger, A. J. High-detectivity polymer photodetectors with spectral response from 300 nm to 1450 nm. *Science* **2009**, *325*, 1665–1667.

[2] Li, N.; Lan, Z. J.; Cai, L. F.; Zhu, F. R. Advances in solution-processable near-infrared phototransistors. *J. Mater. Chem. C* **2019**, *7*, 3711–3729.

[3] Baeg, K. J.; Binda, M.; Natali, D.; Caironi, M.; Noh, Y. Y. Organic light detectors: Photodiodes and phototransistors. *Adv. Mater.* **2013**, *25*, 4267–4295.

[4] Guo, H. T.; Qi, W. H. New materials and designs for 2D-based infrared photodetectors. *Nano Res.* **2023**, *16*, 3074–3103.

[5] Zhang, J.; Itzler, M. A.; Zbinden, H.; Pan, J. W. Advances in InGaAs/InP single-photon detector systems for quantum communication. *Light: Sci. Appl.* **2015**, *4*, e286.

[6] Rong, X.; Wang, X. Q.; Chen, G.; Zheng, X. T.; Wang, P.; Xu, F. J.; Qin, Z. X.; Tang, N.; Chen, Y. H.; Sang, L. W. et al. Mid-infrared photoconductive response in AlGaN/GaN step quantum wells. *Sci. Rep.* **2015**, *5*, 14386.

[7] Yoo, T. J.; Kim, S. Y.; Kwon, M. G.; Kim, C.; Chang, K. E.; Hwang, H. J.; Lee, B. H. A facile method for improving detectivity of graphene/p-type silicon heterojunction photodetector. *Laser Photonics Rev.* **2021**, *15*, 2000557.

[8] Khan, J.; Ahmad, R. T. M.; Tan, J. Y.; Zhang, R. J.; Khan, U.; Liu, B. L. Recent advances in 2D organic-inorganic heterostructures for electronics and optoelectronics. *SmartMat* **2023**, *4*, e1156.

[9] Cong, X. N.; Zheng, Y.; Huang, F.; You, Q.; Tang, J.; Fang, F. E.; Jiang, K.; Han, C.; Shi, Y. M. Efficiently band-tailored type-III van der Waals heterostructure for tunnel diodes and optoelectronic devices. *Nano Res.* **2022**, *15*, 8442–8450.

[10] Xu, Z. H.; He, M.; Wu, Q. K.; Wu, C. C.; Li, X. B.; Liu, B. L.; Tang, M. C.; Yao, J.; Wei, G. D. Ultrafast charge transfer 2D MoS_2/organic heterojunction for sensitive photodetector. *Adv. Sci.* **2023**, *10*, 2207743.

[11] Li, N.; Lei, Y. L.; Miao, Y. Q.; Zhu, F. R. Improved electrical ideality and photoresponse in near-infrared phototransistors realized by bulk heterojunction channels. *iScience* **2022**, *25*, 103711.

[12] Lin, Y. C.; Yang, W. C.; Chiang, Y. C.; Chen, W. C. Recent advances in organic phototransistors: Nonvolatile memory, artificial synapses, and photodetectors. *Small Sci.* **2022**, *2*, 2100109.

[13] Miao, J. L.; Du, M. D.; Fang, Y.; Zhang, X. L.; Zhang, F. J. Photomultiplication type all-polymer photodetectors with single carrier transport property. *Sci. China Chem.* **2019**, *62*, 1619–1624.

[14] Wu, H. N.; Sun, Y. J.; Sun, L. J.; Wang, L. W.; Zhang, X. T.; Hu, W. P. Deep insight into the charge transfer interactions in 1,2,4,5-tetracyanobenzene-phenazine cocrystal. *Chin. Chem. Lett.* **2021**, *32*, 3007–3010.

[15] Tian, X. Z.; Yao, J. R.; Zhang, L. J.; Han, B.; Shi, J. W.; Su, J. W.;

Liu, J.; Li, C. L.; Liu, X. F.; Zhai, T. Y. et al. Few-layered organic single-crystalline heterojunctions for high-performance phototransistors. *Nano Res.* **2022**, *15*, 2667–2673.
[16] Ren, H.; Chen, J. D.; Li, Y. Q.; Tang, J. X. Recent progress in organic photodetectors and their applications. *Adv. Sci.* **2021**, *8*, 2002418.
[17] Ji, S. B.; Wan, C. J.; Wang, T.; Li, Q. S.; Chen, G.; Wang, J. W.; Liu, Z. Y.; Yang, H.; Liu, X. J.; Chen, X. D. Water-resistant conformal hybrid electrodes for aquatic endurable electrocardiographic monitoring. *Adv. Mater.* **2020**, *32*, 2001496.
[18] Wang, Z. L.; Song, X. N.; Jiang, Y.; Zhang, J. D.; Yu, X.; Deng, Y. F.; Han, Y.; Hu, W. P.; Geng, Y. H. A simple structure conjugated polymer for high mobility organic thin film transistors processed from nonchlorinated solvent. *Adv. Sci.* **2019**, *6*, 1902412.
[19] Lee, J.; Ko, S. J.; Seifrid, M.; Lee, H.; Luginbuhl, B. R.; Karki, A.; Ford, M.; Rosenthal, K.; Cho, K.; Nguyen, T. Q. et al. Bandgap narrowing in non-fullerene acceptors: Single atom substitution leads to high optoelectronic response beyond 1000 nm. *Adv. Energy Mater.* **2018**, *8*, 1801212.
[20] Vollbrecht, J.; Lee, J.; Ko, S. J.; Brus, V. V.; Karki, A.; Le, W.; Seifrid, M.; Ford, M. J.; Cho, K.; Bazan, G. C. et al. Design of narrow bandgap non-fullerene acceptors for photovoltaic applications and investigation of non-geminate recombination dynamics. *J. Mater. Chem. C* **2020**, *8*, 15175–15182.
[21] Zhu, Q. H.; Chen, Y. X.; Chen, T. Y.; Zuo, L. J.; Sun, Y. J.; Wang, R.; Xu, M. S. High performance IEICO-4F/WSe_2 heterojunction photodetector based on photoluminescence quenching behavior. *Nano Res.* **2022**, *15*, 8595–8602.
[22] Lee, J.; Ko, S. J.; Lee, H.; Huang, J. F.; Zhu, Z. Y.; Seifrid, M.; Vollbrecht, J.; Brus, V. V.; Karki, A.; Wang, H. B. et al. Side-chain engineering of nonfullerene acceptors for near-infrared organic photodetectors and photovoltaics. *ACS Energy Lett.* **2019**, *4*, 1401–1409.
[23] Bredas, J. L. Mind the gap! *Mater. Horiz.* **2014**, *1*, 17–19.
[24] Du, X. Y.; Zhang, Q.; He, Z. Y.; Lin, H.; Yang, G.; Chen, Z. H.; Zheng, C. J.; Tao, S. L. Performance enhancement in organic solar cells and photodetectors enabled by donor phase optimization at the surface of hole transport layer. *Chin. Chem. Lett.* **2023**, *34*, 107641.
[25] Wei, Z. X.; Zhao, Y. H.; Jiang, J.; Yan, W. B.; Feng, Y. Z.; Ma, J. M. Research progress on hybrid organic-inorganic perovskites for photo-applications. *Chin. Chem. Lett.* **2020**, *31*, 3055–3064.
[26] Wang, S. Y.; Chen, C. S.; Yu, Z. H.; He, Y. L.; Chen, X. Y.; Wan, Q.; Shi, Y.; Zhang, D. W.; Zhou, H.; Wang, X. R. et al. A MoS_2/PTCDA hybrid heterojunction synapse with efficient photoelectric dual modulation and versatility. *Adv. Mater.* **2019**, *31*, 1806227.
[27] He, Z. Y.; Han, J. Y.; Du, X. Y.; Cao, L. Y.; Wang, J.; Zheng, C. J.; Lin, H.; Tao, S. L. Photomemory and pulse monitoring featured solution-processed near-infrared graphene/organic phototransistor with detectivity of 2.4×10^{13} jones. *Adv. Funct. Mater.* **2021**, *31*, 2103988.
[28] Li, D. W.; Du, J. Q.; Tang, Y. J.; Liang, K.; Wang, Y.; Ren, H. H.; Wang, R.; Meng, L.; Zhu, B. W.; Li, Y. F. Flexible and air-stable near-infrared sensors based on solution-processed inorganic–organic hybrid phototransistors. *Adv. Funct. Mater.* **2021**, *31*, 2105887.
[29] Lin, R. X.; Wang, Y. R.; Lu, Q. W.; Tang, B. B.; Li, J. Y.; Gao, H.; Gao, Y.; Li, H. J.; Ding, C. Z.; Wen, J. et al. All-perovskite tandem solar cells with 3D/3D bilayer perovskite heterojunction. *Nature* **2023**, *620*, 994–1000.
[30] Low, J.; Yu, J. G.; Jaroniec, M.; Wageh, S.; Al-Ghamdi, A. A. Heterojunction photocatalysts. *Adv. Mater.* **2017**, *29*, 1601694.
[31] Chen, J. H.; Das, S.; Shao, M.; Li, G. L.; Lian, H. D.; Qin, J.; Browning, J. F.; Keum, J. K.; Uhrig, D.; Gu, G. et al. Phase segregation mechanisms of small molecule-polymer blends unraveled by varying polymer chain architecture. *SmartMat* **2021**, *2*, 367–377.
[32] Yang, B.; Wang, Y.; Li, L.; Zhang, J. Y.; Wang, J. L.; Jiao, H. X.; Hao, D. D.; Guo, P.; Zeng, S.; Hua, Z. K. et al. High performance ternary organic phototransistors with photoresponse up to 2600 nm at room temperature. *Adv. Funct. Mater.* **2021**, *31*, 2103787.
[33] Sheng, Z. H.; Shao, L.; Chen, J. J.; Bao, W. J.; Wang, F. B.; Xia, X. H. Catalyst-free synthesis of nitrogen-doped graphene via thermal annealing graphite oxide with melamine and its excellent electrocatalysis. *ACS Nano* **2011**, *5*, 4350–4358.
[34] Xi, J. B.; Xiao, J. W.; Xiao, F.; Jin, Y. X.; Dong, Y.; Jing, F.; Wang, S. Mussel-inspired functionalization of cotton for nano-catalyst support and its application in a fixed-bed system with high performance. *Sci. Rep.* **2016**, *6*, 21904.
[35] Song, L. F.; Yang, L. P.; Wang, Z.; Liu, D.; Luo, L. Q.; Zhu, X. X.; Xi, Y.; Yang, Z. X.; Han, N.; Wang, F. Y. et al. One-step electrospun SnO_2/MO_x heterostructured nanomaterials for highly selective gas sensor array integration. *Sens. Actuat. B: Chem.* **2019**, *283*, 793–801.
[36] Yurash, B.; Cao, D. X.; Brus, V. V.; Leifert, D.; Wang, M.; Dixon, A.; Seifrid, M.; Mansour, A. E.; Lungwitz, D.; Liu, T. et al. Towards understanding the doping mechanism of organic semiconductors by Lewis acids. *Nat. Mater.* **2019**, *18*, 1327–1334.
[37] Nguyen, L. H.; Hoppe, H.; Erb, T.; Günes, S.; Gobsch, G.; Sariciftci, N. S. Effects of annealing on the nanomorphology and performance of poly(alkylthiophene): Fullerene bulk-heterojunction solar cells. *Adv. Funct. Mater.* **2007**, *17*, 1071–1078.
[38] Han, T.; Wang, Z. J.; Shen, N.; Zhou, Z. W.; Hou, X. H.; Ding, S. F.; Jiang, C. Z.; Huang, X. Y.; Zhang, X. F.; Liu, L. L. Diffusion interface layer controlling the acceptor phase of bilayer near-infrared polymer phototransistors with ultrahigh photosensitivity. *Nat. Commun.* **2022**, *13*, 1332.
[39] Giri, G.; Verploegen, E.; Mannsfeld, S. C. B.; Atahan-Evrenk, S.; Kim, D. H.; Lee, S. Y.; Becerril, H. A.; Aspuru-Guzik, A.; Toney, M. F.; Bao, Z. N. Tuning charge transport in solution-sheared organic semiconductors using lattice strain. *Nature* **2011**, *480*, 504–508.
[40] Xue, G. B.; Zhao, X. K.; Qu, G.; Xu, T. B.; Gumyusenge, A.; Zhang, Z. R.; Zhao, Y.; Diao, Y.; Li, H. Y.; Mei, J. G. Symmetry breaking in side chains leading to mixed orientations and improved charge transport in isoindigo-*alt*-bithiophene based polymer thin films. *ACS Appl. Mater. Interfaces* **2017**, *9*, 25426–25433.
[41] Zhao, X. K.; Xue, G. B.; Qu, G.; Singhania, V.; Zhao, Y.; Butrouna, K.; Gumyusenge, A.; Diao, Y.; Graham, K. R.; Li, H. Y. et al. Complementary semiconducting polymer blends: Influence of side chains of matrix polymers. *Macromolecules* **2017**, *50*, 6202–6209.
[42] Iqbal, M. A.; Liaqat, A.; Hussain, S.; Wang, X. S.; Tahir, M.; Urooj, Z.; Xie, L. M. Ultralow-transition-energy organic complex on graphene for high-performance shortwave infrared photodetection. *Adv. Mater.* **2020**, *32*, 2002628.
[43] Buscema, M.; Island, J. O.; Groenendijk, D. J.; Blanter, S. I.; Steele, G. A.; van der Zant, H. S. J.; Castellanos-Gomez, A. Photocurrent generation with two-dimensional van der Waals semiconductors. *Chem. Soc. Rev.* **2015**, *44*, 3691–3718.
[44] Shidachi, R.; Jinno, H.; Lee, S.; Yokota, T.; Someya, T. Suppressing dark current in organic phototransistors through modulating electron injection via a deep work function electrode. *ACS Appl. Electron. Mater.* **2019**, *1*, 1054–1058.
[45] Jang, W.; Kim, B. G.; Seo, S.; Shawky, A.; Kim, M. S.; Kim, K.; Mikladal, B.; Kauppinen, E. I.; Maruyama, S.; Jeon, I. et al. Strong dark current suppression in flexible organic photodetectors by carbon nanotube transparent electrodes. *Nano Today* **2021**, *37*, 101081.
[46] Günes, S.; Neugebauer, H.; Sariciftci, N. S. Conjugated polymer-based organic solar cells. *Chem. Rev.* **2007**, *107*, 1324–1338.
[47] Guo, Y. L.; Du, C. Y.; Di, C. A.; Zheng, J.; Sun, X. N.; Wen, Y. G.; Zhang, L.; Wu, W. P.; Yu, G.; Liu, Y. Q. Field dependent and high light sensitive organic phototransistors based on linear asymmetric organic semiconductor. *Appl. Phys. Lett.* **2009**, *94*, 143303.
[48] Chow, P. C. Y.; Matsuhisa, N.; Zalar, P.; Koizumi, M.; Yokota, T.; Someya, T. Dual-gate organic phototransistor with high-gain and linear photoresponse. *Nat. Commun.* **2018**, *9*, 4546.
[49] Zhao, Z. J.; Li, C. L.; Shen, L.; Zhang, X. L.; Zhang, F. J. Photomultiplication type organic photodetectors based on electron tunneling injection. *Nanoscale* **2020**, *12*, 1091–1099.
[50] Du, B. C.; Yi, J. C.; Yan, H.; Wang, T. Temperature induced aggregation of organic semiconductors. *Chem.—Eur. J.* **2021**, *27*, 2908–2919.

[51] Maturová, K.; van Bavel, S. S.; Wienk, M. M.; Janssen, R. A. J.; Kemerink, M. Description of the morphology dependent charge transport and performance of polymer: Fullerene bulk heterojunction solar cells. *Adv. Funct. Mater.* **2011**, *21*, 261–269.

[52] Cho, M. Y.; Kim, S. J.; Han, Y. D.; Park, D. H.; Kim, K. H.; Choi, D. H.; Joo, J. Highly sensitive, photocontrolled, organic thin-film transistors using soluble star-shaped conjugated molecules. *Adv. Funct. Mater.* **2008**, *18*, 2905–2912.

[53] Chen, H. L.; Cheng, N. Y.; Ma, W.; Li, M. L.; Hu, S. X.; Gu, L.; Meng, S.; Guo, X. F. Design of a photoactive hybrid bilayer dielectric for flexible nonvolatile organic memory transistors. *ACS Nano* **2016**, *10*, 436–445.

[54] Snyder, P. J.; Kirste, R.; Collazo, R.; Ivanisevic, A. Persistent photoconductivity, nanoscale topography, and chemical functionalization can collectively influence the behavior of PC12 cells on wide bandgap semiconductor surfaces. *Small* **2017**, *13*, 1700481.

[55] Chua, L. L.; Zaumseil, J.; Chang, J. F.; Ou, E. C. W.; Ho, P. K. H.; Sirringhaus, H.; Friend, R. H. General observation of n-type field-effect behaviour in organic semiconductors. *Nature* **2005**, *434*, 194–199.

[56] Nam, S.; Han, H.; Seo, J.; Song, M.; Kim, H.; Anthopoulos, T. D.; McCulloch, I.; Bradley, D. D. C.; Kim, Y. Ambipolar organic phototransistors with p-type/n-type conjugated polymer bulk heterojunction light-sensing layers. *Adv. Electron. Mater.* **2016**, *2*, 1600264.

[57] Zhu, W. G.; Yi, Y. P.; Zhen, Y. G.; Hu, W. P. Precisely tailoring the stoichiometric stacking of perylene-TCNQ co-crystals towards different nano and microstructures with varied optoelectronic performances. *Small* **2015**, *11*, 2150–2156.

[58] Ito, Y.; Virkar, A. A.; Mannsfeld, S.; Oh, J. H.; Toney, M.; Locklin, J.; Bao, Z. N. Crystalline ultrasmooth self-assembled monolayers of alkylsilanes for organic field-effect transistors. *J. Am. Chem. Soc.* **2009**, *131*, 9396–9404.

[59] Zhu, W. G.; Sun, Y. J.; Liu, J.; Bai, S. M.; Zhang, Z. C.; Shi, Q.; Hu, W. P.; Fu, H. B. Exciton transport in molecular semiconductor crystals for spin-optoelectronics paradigm. *Chem.—Eur. J.* **2021**, *27*, 222–227.

[60] Newman, C. R.; Frisbie, C. D.; da Silva Filho, D. A.; Brédas, J. L.; Ewbank, P. C.; Mann, K. R. Introduction to organic thin film transistors and design of n-channel organic semiconductors. *Chem. Mater.* **2004**, *16*, 4436–4451.

[61] Kafourou, P.; Nugraha, M. I.; Nikitaras, A.; Tan, L. X.; Firdaus, Y.; Aniés, F.; Eisner, F.; Ding, B. W.; Wenzel, J.; Holicky, M. et al. Near-IR absorbing molecular semiconductors incorporating cyanated benzothiadiazole acceptors for high-performance semitransparent n-type organic field-effect transistors. *ACS Mater. Lett.* **2022**, *4*, 165–174.

[62] Fu, B. B.; Sun, L. J.; Liu, L.; Ji, D. Y.; Zhang, X. T.; Yang, F. X.; Hu, W. P. Low-power high-mobility organic single-crystal field-effect transistor. *Sci. China Mater.* **2022**, *65*, 2779–2785.

[63] Nam, S.; Seo, J.; Han, H.; Kim, H.; Bradley, D. D. C.; Kim, Y. Efficient deep red light-sensing all-polymer phototransistors with p-type/n-type conjugated polymer bulk heterojunction layers. *ACS Appl. Mater. Interfaces* **2017**, *9*, 14983–14989.

[64] Kim, S.; Lee, D.; Lee, J.; Cho, Y.; Kang, S. H.; Choi, W.; Oh, J. H.; Yang, C. Diazapentalene-containing ultralow-band-gap copolymers for high-performance near-infrared organic phototransistors. *Chem. Mater.* **2021**, *33*, 7499–7508.

[65] Han, J. Y.; Wang, J.; Yang, M.; Kong, X.; Chen, X. Q.; Huang, Z. H.; Guo, H.; Gou, J.; Tao, S. L.; Liu, Z. J. et al. Graphene/organic semiconductor heterojunction phototransistors with broadband and Bi-directional photoresponse. *Adv. Mater.* **2018**, *30*, 1804020.